JAST, Vol. 2, No. 4, pp 9–26

JAST
Journal of Aerospace Science and Technology

Effect of Amplitude and Mean Angle of Attack on the Unsteady Surface Pressure of a Pitching Airfoil

M. R. Soltani[1], A. Bakhshalipour[2], M. Seddighi[3]

Details of pressure distributions on a two dimensional airfoil oscillating in pitch through the stall in a 0.8 × 0.8 m² low-speed wind tunnel are presented. Pitching occurred around the airfoils quarter-chord axis. Pitch rate, Reynolds number, and oscillation amplitudes were varied to determine the effects on pressure and lift distributions. It was found that the mean angle of attack and pitching amplitude had strong effects on the flow field hence pressure distribution in the immediate vicinity of the airfoil leading edge, $\frac{x}{c} \leq 0.4$. For pressure ports located at $\frac{x}{c} > 0.4$, the aforementioned effects were not strong. It seems that during the oscillatory motions the flow was mostly separated. This investigation shows weak unsteady effects when the maximum dynamic angle of attack was below that of the static stall; i.e. $\alpha_{\max.dynamic} \leq \alpha_{\max.static}$. For higher angles of attack, strong unsteady effects appear, which depend on the mean angle of attack, frequency and amplitude of the oscillation. Dynamic stall and dynamic reattachment contribute to a favorable effect of unsteadiness on the surface pressure signature and hence the mean lift coefficient which increases as compared to the steady state lift and pressure data.

NOMENCLATURE

C_l	Lift coefficient
C	airfoil chord
$C_p = \frac{p - p_\infty}{q_\infty}$	Pressure coefficient
P	Surface static pressure
p_∞	Free stream static pressure
q_∞	Free stream dynamic pressure
U_∞	Free stream velocity
A	Amplitude
K	Reduced frequency; $= \frac{\omega c}{2U_\infty}$
f	Oscillation frequency (hz)
τ	t/T non-dimensional time
α	Angle of attack (deg)
α_{mean}	Mean angle of attack (deg)
$\bar{\alpha}$	Non-dimensional angle of attack

1. *Associate Professor, Dept. of Aerospace Eng., Sharif Univ. of Tech., Tehran, Iran, Email: msoltani@sharif.edu*
2. *Ph.D. Candidate, Dept. of Aerospace Eng., Sharif Univ. of Tech., Tehran, Iran.*
3. *Graduate Student, Dept. of Aerospace Eng., Sharif Univ. of Tech., Tehran, Iran.*

INTRODUCTION

The energetic nature of the unsteady flow fields has been a topic of study for decades. Because of their complicated, rapidly changing time dependent nature, significant amount of both theoretical and experimental research has been conducted to understand the fluid mechanics of these flow fields [1-3]. Furthermore, with the continuing development of high-performance aircraft and helicopter, dynamic stall and blade stall flutter have been of increasing concern. A few other examples are the flows generated by devices such as turbo machines and wind turbine blades, which have received considerable attentions in recent years [4-7].

Many of the aerodynamic phenomena governing the behavior of wind turbine blades are known, but the details of the flow are still poorly understood and need to be predicted accurately. As a result of this inaccuracy, the actual loading, and therefore the power

outputs of the wind turbines are consistently under predicted. For most situations, steady-state, two-dimensional wind turbine data are used to estimate the loads on blades, which is then used to calculate structural loading and power output [7-10]. This inadequate prediction leads to a failure in the power generation, gear box, and even turbine blades. Because the corresponding loading and power output is caused by aerodynamic forces which are directly controlled by the associated unsteady flows, a better understanding of the fluid dynamics is essential if accurate modeling of the rotor aerodynamics and acceptable prediction of the turbine loads and power generation are to be made. Horizontal axis wind turbine (HAWT) rotors experience unsteady aerodynamics due to wind shear when the rotor is yawed, or when the rotor blades pass through the support tower wake or when the wind is gusting. An understanding of this unsteady behavior is necessary to assist the design of new rotor airfoil. Although there is extensive information on forced unsteady surface pressure and the corresponding aerodynamic loads on two and three dimensional airfoils undergoing various motions, more experimental data are still needed to gain a clear understanding of the fluid mechanics of the flow behavior over the airfoils pitching at various rates and at various angles of attack. Furthermore, the existing experimental and theoretical data deal with the overall surface pressure distribution and /or aerodynamic loads. It is therefore, the intent of the present research to provide a set of detailed and accurate pressure signatures on an airfoil used in a section of HAWT rotor undergoing sinusoidal oscillation in the angle of attack. The experimental result will include static and dynamic pressure data at each port. As noted by Leishman [4], it is hoped that these wind tunnel results as well as other existing data will provide an opportunity to better understand the physics of wind turbine aerodynamics, and provide a definitive data source for validating predictive methods, hence solving some of the present challenges.

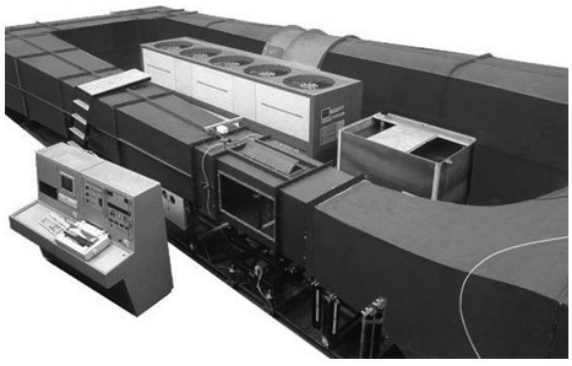

Figure 1. Schematic of the wind tunnel

EXPERIMENTAL FACILITY

All tests were conducted in the subsonic wind tunnel of Jahad Research Center in Iran. A schematic of the tunnel and the overall test set up is shown in Figure 1. The tunnel is of closed return type, and has a test section of approximately 80 cm wide, 80 cm high, and 200 cm long, which operates at speeds between 10 and 100 m/sec. at Reynolds number of up to 5.26×10^6 per meter. The inlet of the tunnel has a 7:1 contraction ratio with four large, anti-turbulence screens and honeycomb in its settling chamber to reduce tunnel turbulence to less than 0.1% the test section at all speeds [11]. A 25 cm constant chord airfoil model was designed and manufactured for the test program. Figure 2 shows the airfoil section along with the 64 pressure ports located on its upper and lower surfaces used for static and dynamic pressure measurements. The airfoil is used in a section of 660 kW horizontal axis wind turbine blade. The pressure ports are located along the chord at an angle of 20 degrees with respect to the model span (Figure 2). The pitch rotation point was fixed at about the wing quarter chord. Due to the high number of pressure ports, 64, and the size of the selected pressure transducers, we could not place the transducers inside the model. Therefore, extensive experiments were conducted to ensure that the time taken for the pressure to reach the transducers is much less than the frequency response of the transducers themselves [12,13]. The oscillating system was able to pitch the model at various amplitudes, mean angles of attack and reduced frequency K. For steady state tests, the model was set to an angle of attack and the tunnel conditions were adjusted. At the operator's request, pressure measurements from the airfoil surface taps and all other channels of information were obtained and stored or reduced for checkup. The angles of attack for the steady case were always from 0 to -10 degrees and then from 0 to 25 degrees and back to zero.

For the dynamic tests, the tunnel conditions were set while the model was stationary at the desired mean angle of attack. The oscillation system was started and the model was allowed to oscillate through several cycles to establish the flow filed. At the operator's request, the model surface pressure and tunnel condition data were all acquired simultaneously.

Data were acquired and processed from the 64 surface pressure taps, 2 individual tunnel pressure transducers, and an angle of attack potentiometer using two analog to digital boards. One was a 12 bit, 64 channel National Instrument Board capable of a sample rate of 500 kHz for measuring the model surface pressure, and the other board was a 16 bit 16 channel used for measuring the tunnel velocity and the model angle of attack. Dynamic oscillatory data were then digitally filtered using various cut-off

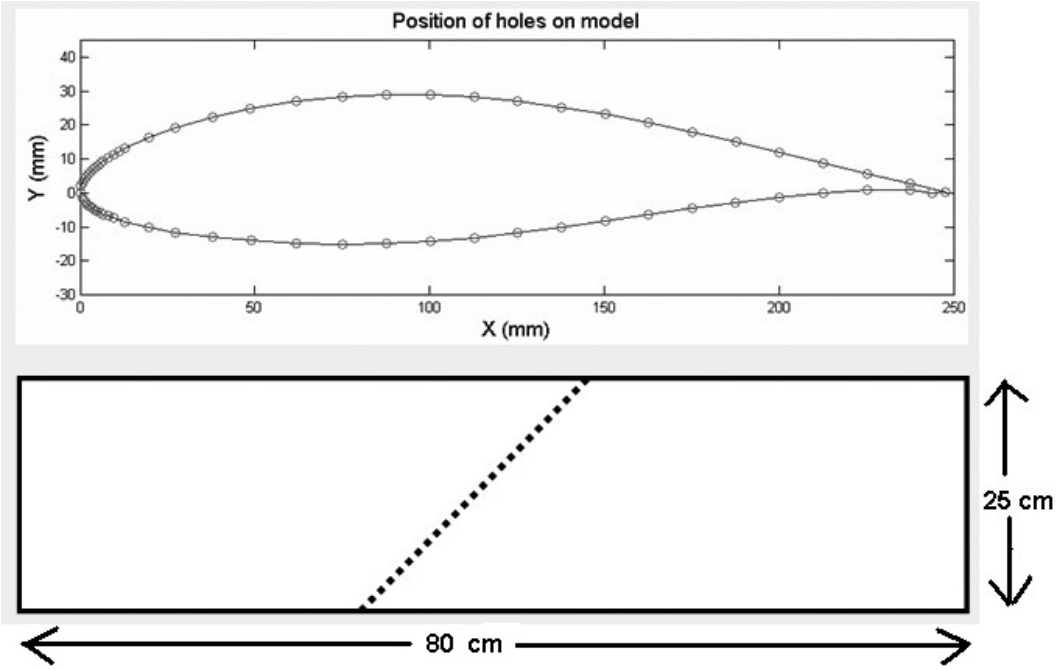

Figure 2. Airfoil section and location of pressure ports.

and transition frequencies to find the best frequencies to fit the original data. The filtering process was necessary to eliminate the oscillatory signals form the data which were caused by the electrical noise, linkages etc. Note that the acquisition frequency and the sample rate for both A/D boards were similar while other parameters were set such that both boards operate similarly through various tests that were conducted prior to final tests.

Finally, all static data were corrected for the solid tunnel sidewalls, and the wake blockage effects using the method explained in Reference [14]. For the oscillatory data, however, there is no method available to correct the data. Therefore, all dynamic data were corrected using only the static methods explained in Reference [14]. For the dynamic case, the model was oscillating and the data for all the ports were collected when the tunnel was off. The oscillation frequency as well as the acquisition constants were exactly equal to those during tunnel on conditions. All pressure data acquired during the tunnel on condition were subtracted from those obtained during the tunnel off situation to account for the inertial effects.

RESULTS AND DISCUSSION

As mentioned before, the main purpose of this experimental work is to examine the behavior of pressure at various locations of the airfoil, 64 ports, undergoing sinusoidal pitch oscillation at low to high angles of attack and at various reduced frequencies. Static data were also recorded as a baseline. Both static and oscillatory tests were conducted at Reynolds numbers of $0.4 \times 10^{6} < R_e < 1.3 \times 10^{6}$.

The airfoil used for this investigation was a section of a horizontal axis wind turbine blade capable of producing 660 kW electricity and similar to that of the NACA 6 series airfoils; however, no experimental or theoretical data (static or dynamic) are available for this airfoil. The test defined baseline conditions for steady state angles of attack from -10 degrees to 25 degrees and examined unsteady behaviors by oscillating the model about its quarter chord axis for different mean angles of attack, reduced frequencies, and amplitudes. All tests were conducted at the aforementioned Reynolds numbers. In this paper, the oscillatory data for surface pressure variation at different mean angles of attack and amplitudes for a constant reduced frequency of K= 0.04 will be presented. Static data for different Reynolds numbers and various leading- edge roughnesses are presented in Reference [12]. The effect of reduced frequency on the dynamic pressure distributions will be presented later. Figure 3 shows both static and dynamic variations of C_p at the leading edge with the non-dimensional time and angle of attack for a reduced frequency of 0.04, three different mean angles of attack, and two different amplitudes. The amplitude and mean angles of attack were selected such that during one oscillation cycle, the model would oscillate below static stall angles of attack, near stall, or beyond the static stall angle of attack. This will enable us to compare the differences

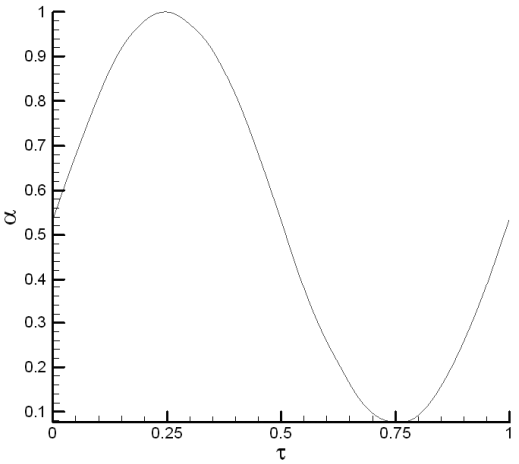

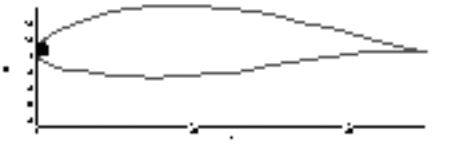

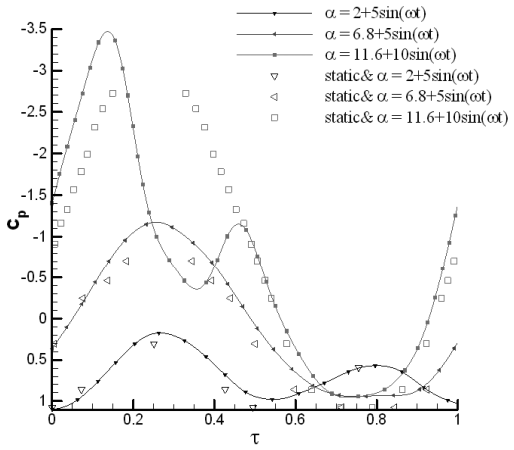

(a) variations of C_p with τ

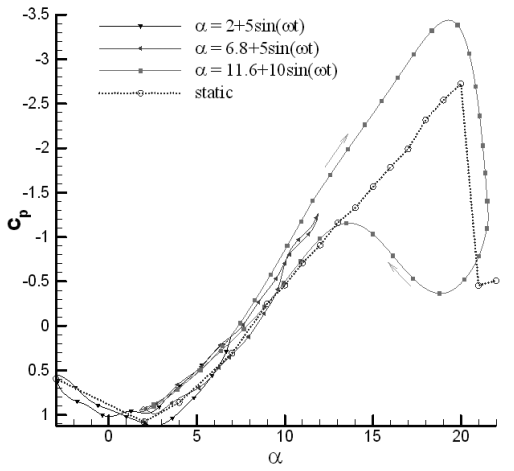

(b) variations of C_p with α

Figure 3. Static and dynamic variations of pressure for the leading edge, x/c=0, port.

in the pressure variations for each port undergoing different maximum and minimum angles of attack. Static data for all cases are shown in the C_p vs. τ plot, Figure 3a, while for the C_p vs. alpha curve, Figure 3b, only a single static curve is shown as it should be. Furthermore, variations of the angle of attack with time along with a drawing of the model with location of the pressure port under study are shown in this figure too.

Static pressure signature data for this port, $\frac{x}{c} = 0$ shows a linear increase in the $|C_p|$ from $\alpha \cong 2$ ° to $\alpha \cong 20$ ° angles of attack and $C_p = 0$ at $\alpha \cong 8$ °. Maximum C_p for the static case occurs at $\alpha \cong 20$ ° (Figure 3b), which indicate that flow remains attached to this port up to this angle of attack. By further increasing the angle of attack, $\alpha > 20$ °, $|C_p|$ drops sharply and remains almost constant up to 22 ° angle of attack (Figure 3b). By examining variations of the pressure with τ, Figure 3a, it is clearly seen that for the lowest amplitude and mean angles of attack case, $\alpha = 2 + 5\sin(\omega t)$, static data lead their corresponding dynamic values for most of the upstroke motion and lag during the entire downstroke portion. Similar situation is seen for the next case, $\alpha = 6.8 + 5\sin(\omega t)$ where C_p lags the static data in the upstroke motion up to about 9 degrees angle of attack and starts to lead for the rest of the motion. Variations of C_p with τ for both of the aforementioned cases are almost sinusoidal, which may indicate that no flow separation has occurred and flow field behaves like potential flow does, Figure 3a. However, for the highest mean angle of attack and amplitude shown here, $\alpha = 11.6 + 10\sin(\omega t)$, the situation differs. As seen by inspection, static data lags the dynamic ones in the upstroke motion, but leads in the downstroke portion (Figure 3a), however, in the downstroke motion, the differences in the absolute values of C_p vs. τ for all τ's are much more than similar cases mentioned above. These variations are shown in the lower figure, C_p vs. angle of attack (Figure 3b). The differences in the C_p values for the upstroke and downstroke motions create a hysteresis loop where its shape is a strong function of the mean angles of attack, oscillation amplitude, and reduced frequency. Variations of C_p vs. α show that the hysteresis loops for the first two cases, where $\alpha_{\max}$ is smaller than the static stall angle of attack for this port, are narrow and follow static data in the upstroke motions. While in the downstroke motions, the dynamic data are higher than their corresponding static values (Figure 3b). For the highest mean angle of attack and amplitude case, C_p vs. α data shows that in the upstroke motion, dynamic data lead static ones slightly while in the downstroke portion of the motion, $|C_p|$ is much less than the corresponding static ones until the angle of attack is reduced to about 13 degrees. From this angle of attack, α=13 ° , down to α=8 ° , both static and dynamic data are almost identical as seen in (Figures.3a and

3b). The dynamic C_p , lead its static data for the rest of the motion, α=8 to α= -16 degrees.

Figure 4 shows static and dynamic variations of pressure with τ and α for the x/c =0.02 ports for the upper and lower surfaces respectively. Again variations of alpha vs. τ and a drawing of the model along with the pressure ports under study are shown for clarity. Static data for all cases are shown for comparison. It is seen by inspection that in contrast to Figure 3, static C_p for the upper surface (Figure 4b), varies non- linearly with alpha and stalls at a slightly lower angle of attack than that of Figure 3. For the lower surface, however, static C_p increase up to $\alpha \cong 12$ ° and decreases slightly as alpha increase (Figure 4d). Variations of C_p vs. τ for both ports are similar to those in Figure 3, leading edge port. However, absolute values of C_p for the upper port for all motions examined in this figure (Figure 4a), are much higher than those of Figure 3. Furthermore, for the $\alpha = 11.6 + 10\sin(\omega t)$ case, and in the upstroke motion, Figure 4 shows that the dynamic $|C_p|$ for both ports is at first lower than its corresponding static values, (Figure 4b and 4d), and leads static data as higher alpha is reached. Variations of C_p vs. α for the upper port (Figure 4b), show a wider hysteresis loop during the entire motion for both low alpha cases when compared with similar cases in Figure 3. Dynamic C_p 's are lower than the static ones in the upstroke motions for all three cases examined in this figure, however, during the downstroke motion a lead in the dynamic data for all angles of attack is observed. moreover, the shape of the hysteresis loop for the lowest α_{mean} is of an ellipsoidal shape (Figure 4b). A similar trend is seen for the next case, $\alpha_{mean} =$ 6.8 ° , however, static data for this motion lags the corresponding dynamic data for angles of attack of 9 degrees and above in the upstroke motion. For the highest α_{mean} and amplitude case, variations of C_p vs. α is somehow different than the other two cases examined before (Figure 4b). It is seen by inspection that the dynamic C_p 's for this case lags the static one up to an angle of attack of about 12 degrees and leads for the rest of the upstroke motion until $\alpha_{\max}$ is reached. In the downstroke motion, C_p lags its corresponding static values until an angle of attack of about 9 degrees below where the dynamic $|C_p|$ are higher than the analogous static ones (Figure 4b). These variations of C_p with alpha form a figure eight shape where one portion of it falls in the low alpha case and behaves similar to the first two cases examined before, and the other portion falls in the stall range, the high alpha portion of the motion. The hysteresis loop in the high alpha case is wide and seems that it does not have a simple geometrical shape, while that of the low alpha one is similar to an ellipsis and is narrow (Figure 4b). For the lower surface pressure port, the dynamic C_p 's lag static ones when α increases and lead when α decreases (Figure 4d). The hysteresis loops for the lower pressure port for all cases are narrow; however, their shapes are similar to that of the upper surface one Figure 4d.

Figures 5 and 6 show static and dynamic variations of C_p for both upper and lower surfaces for pressure ports located at $\frac{x}{c} = 0.05$ and $\frac{x}{c} = 0.15$, respectively. Again static data for all cases are shown for comparison. From these figures it is clearly seen that as $\frac{x}{c}$ increases, the static values of $|C_{p_{\max}}|$ for the corresponding port decreases and flow separations reaches the port at a smaller angle of attack. For example, for the port located at $\frac{x}{c} = 0.15$, $|C_{p_{\max}}|$ occurs at $\alpha \cong 12$ degrees (Figure 6b), while for the $\frac{x}{c} = 0.05$ port (Figure 5b), it occurs at $\alpha \cong 15.5$ degrees. In contrast to the leading-edge ports (Figure 3), variations of static C_p with alpha for those ports are non-linear with softer stall characteristics (Figure 5b, Figure 6b).

For the lower surface case, similar trends are observed (Figure 5d and 6d). Variations of static C_p for the lower surface ports start at negative values and increase as alpha increases (Figure 5d, Figure 6d). For both pressure ports $|C_{p_{\max}}|$ occurs at about 20 degrees angle of attack, beyond which their values decrease as seen from these figures. Dynamic variations of C_p with alpha for these ports, $\frac{x}{c} = 0.05$ and $\frac{x}{c} = 0.15$, show a similar behavior as seen for the $\frac{x}{c} = 0.02$ port, however, $|C_{p_{\max}}|$ for these ports (Figures 5b, 6b), are much lower than those in Figure 4. For the lowest α_{mean} , the shapes of the hysteresis loops for both ports are similar, but their values are not the same (Figures 5b and 6b). Further, $|C_p|$ for this α_{mean} and for the port located at $\frac{x}{c} = 0.15$ (Figure 6b), leads its corresponding static value in the upstroke motion in contrast to the similar cases for the $\frac{x}{c} = 0.02$ and $\frac{x}{c} = 0.05$ ports. In the downstroke motion, dynamic $|C_p|$ leads the static values for all cases examined here. For the $\alpha_{mean} = 6.8$ degrees case, Figure 6b shows that the dynamic hysteresis loops forms a figure eight shape and $|C_{p_{\max}}|$ for this motion is slightly higher than that of the static case.

For the highest mean angles of attack and amplitude cases, figures 5b and 6b show that dynamic variations of C_p with alpha form figure eight shapes as seen before, but the cross over angle is smaller than that in Figure 4. The width of the hysteresis loops for the low alpha portion of the motion is narrow while that of the high alpha portion is wide, (Figures 5b and 6b,i).

The behaviors of dynamic C_p for the lower surface pressure ports (Figures 5d and 6d), are similar to those of $\frac{x}{c} = 0.02$ port for the first two cases, $\alpha_{mean} = 2$ and 6.8 degrees. However, for the highest α_{mean} case, the hysteresis loops for both ports are wider than in Figure 4. Moreover, the hysteresis loops for both ports form figure eight shapes, but the cross over angles is

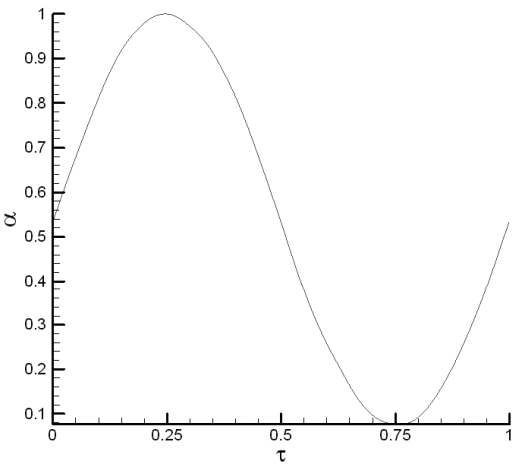

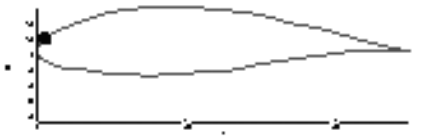

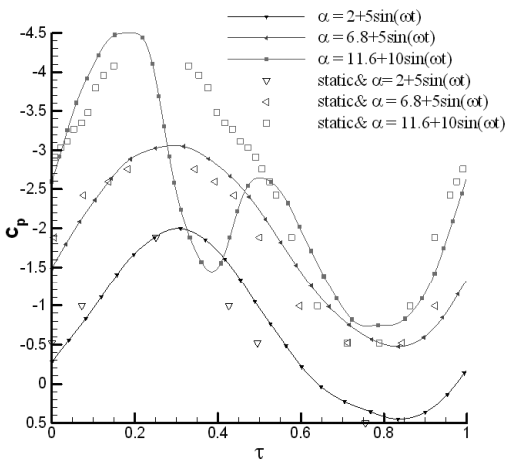

(a) variations of C_p vs τ

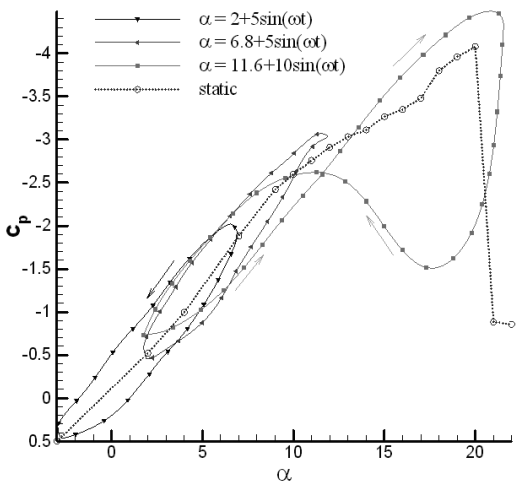

(b) variation of C_p vs α

i) upper

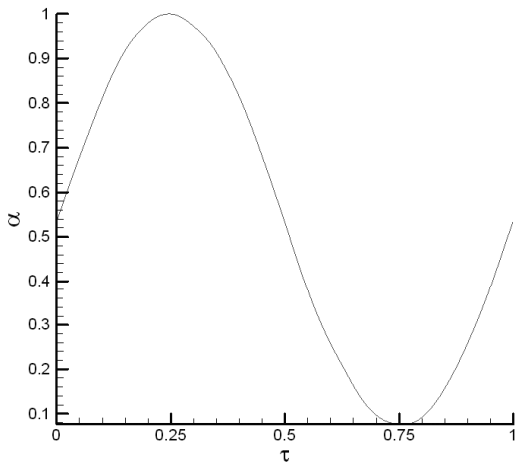

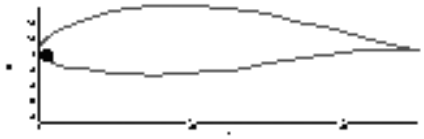

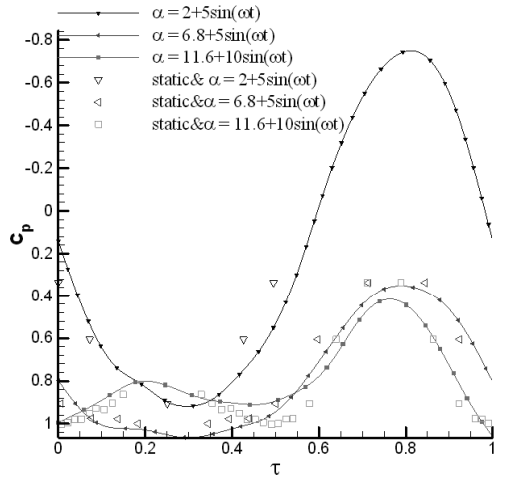

(c) variation of C_p vs τ

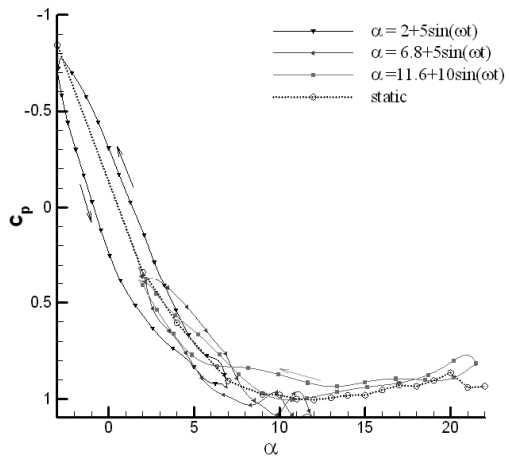

(d) variation of C_p vs α

ii) lower

Figure 4. Static and dynamic variations of pressure for the x/c=0.02 ports.

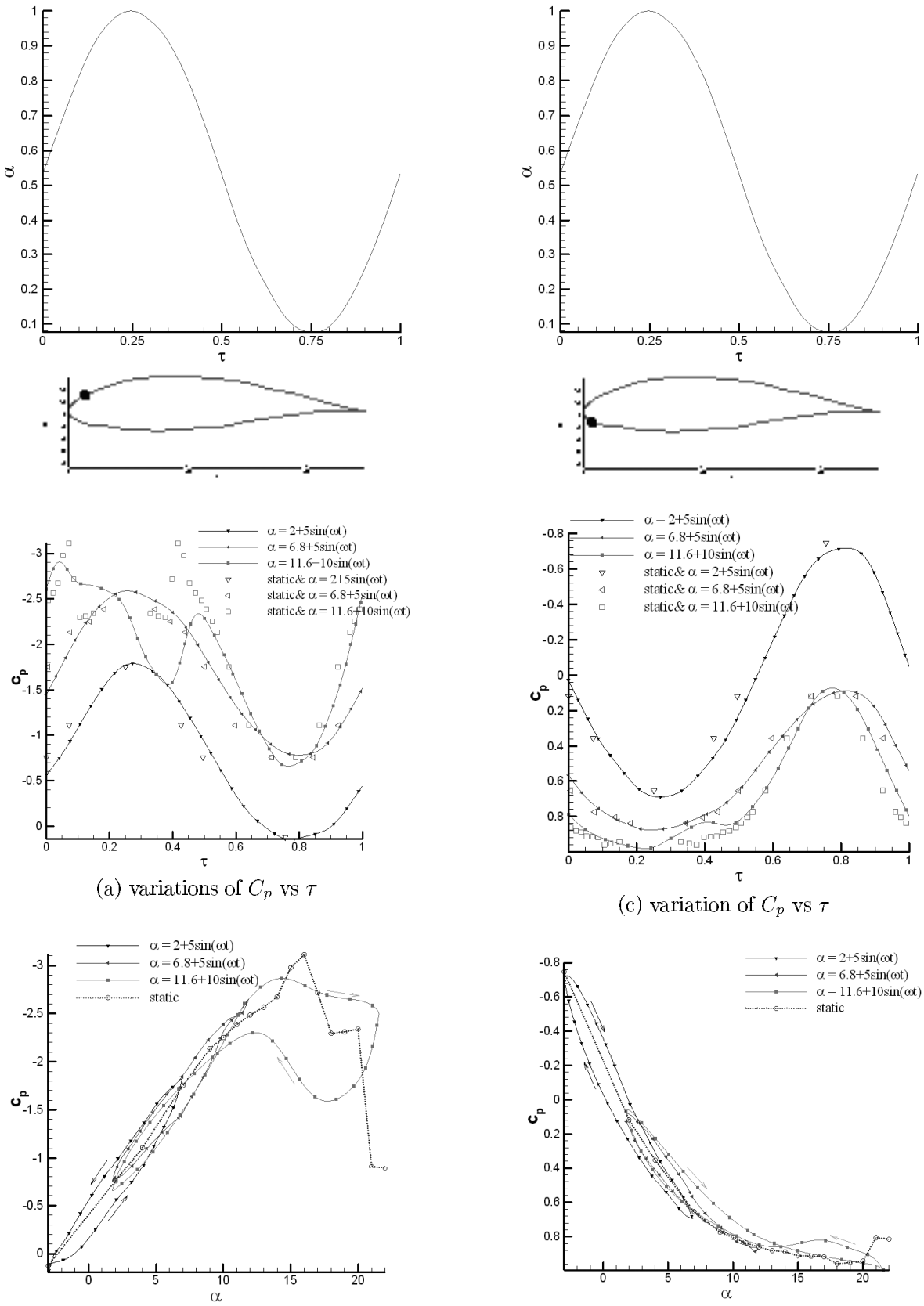

(a) variations of C_p vs τ

(c) variation of C_p vs τ

(b) variation of C_p vs α
i) upper

(d) variation of C_p vs α
ii) lower

Figure 5. Static and dynamic variations of pressure for the x/c=0.05 ports.

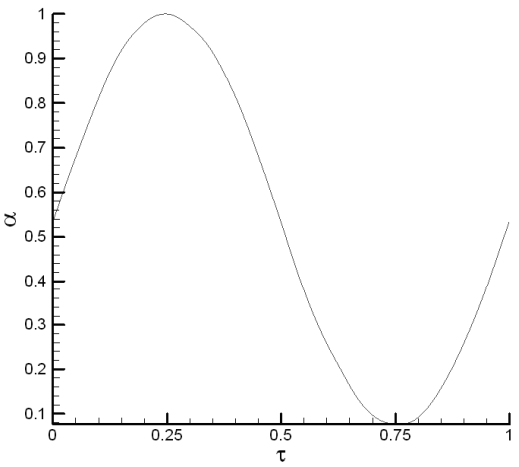

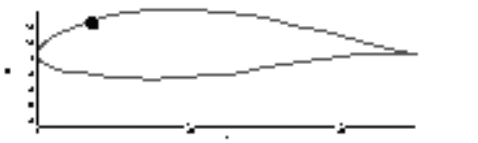

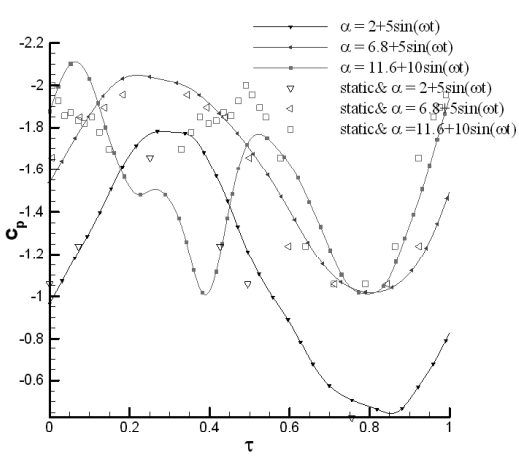

(a) variations of C_p vs τ

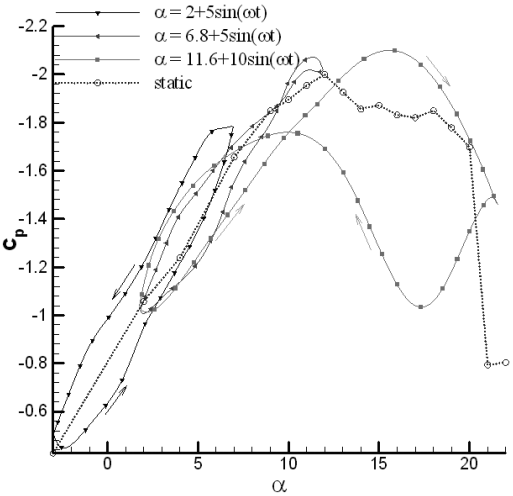

(b) variation of C_p vs α
i) upper

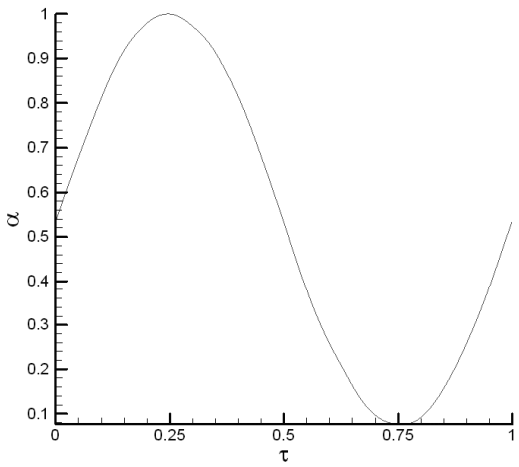

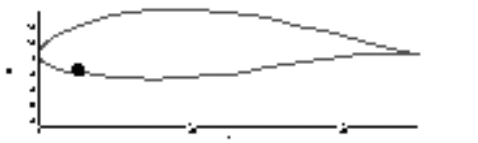

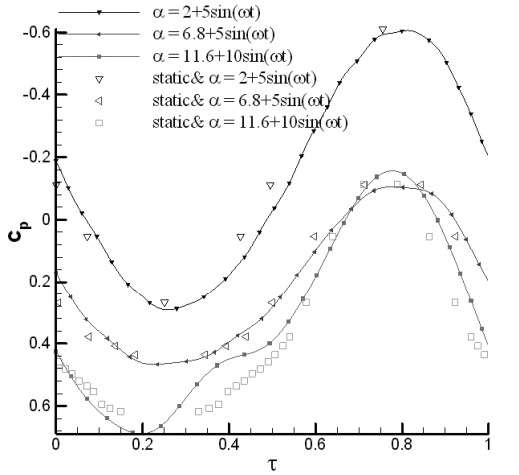

(c) variation of C_p vs τ

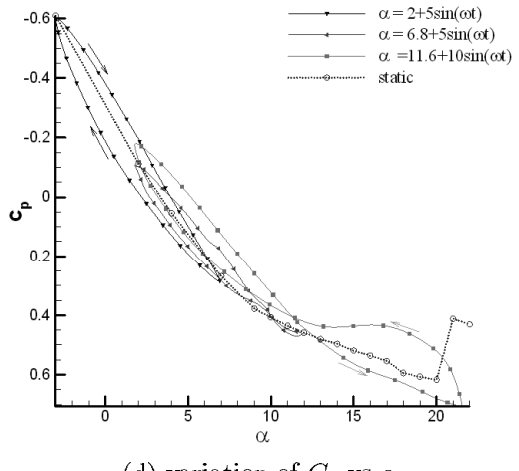

(d) variation of C_p vs α
ii) lower

Figure 6. Static and dynamic variations of pressure for the x/c=0.15 ports.

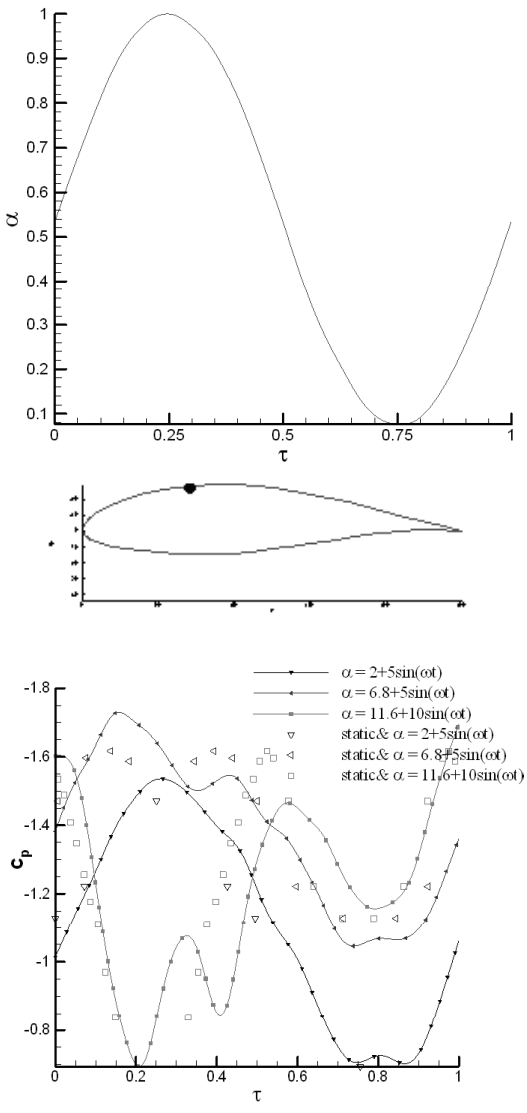

(a) variations of C_p vs τ

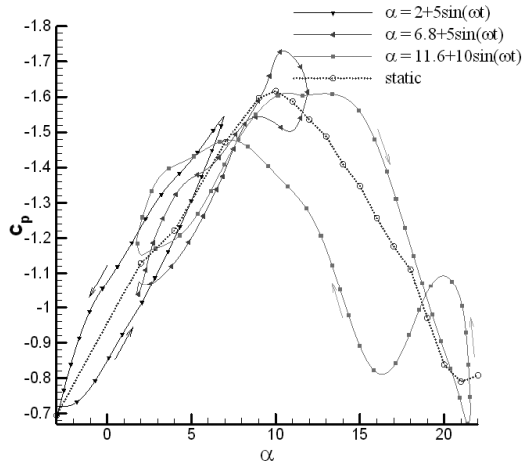

(b) variation of C_p vs α

i) upper

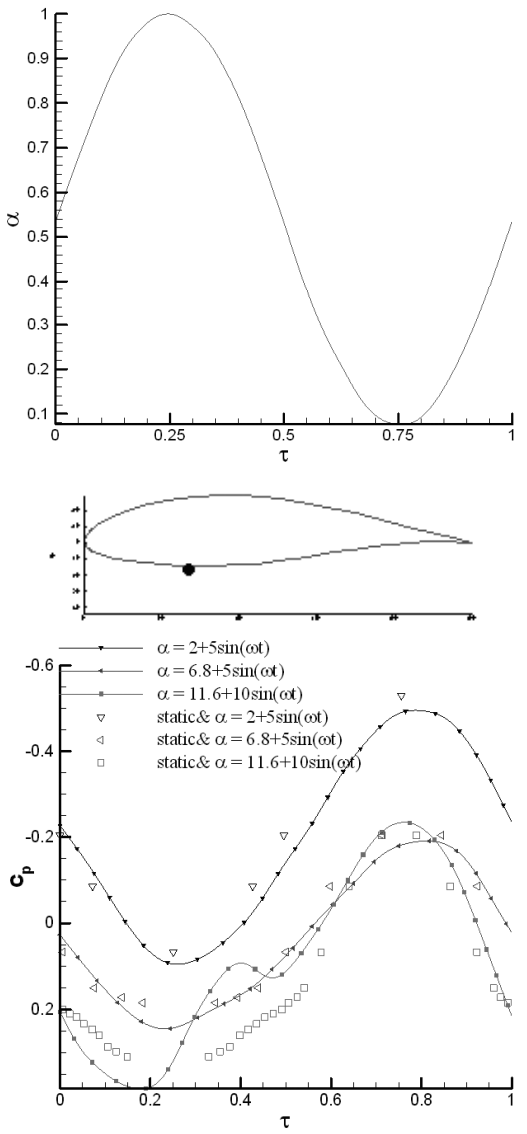

(c) variation of C_p vs τ

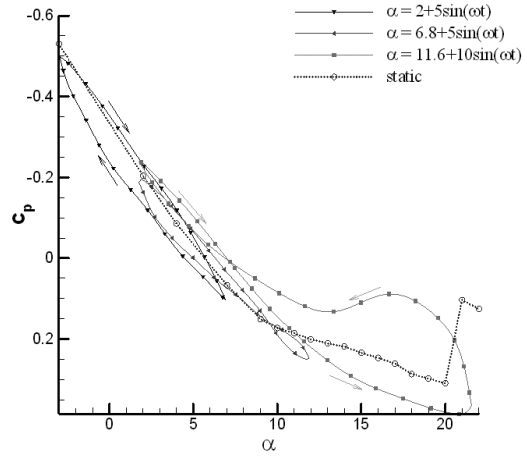

(d) variation of C_p vs α

ii) lower

Figure 7. Static and dynamic variations of pressure for the x/c=0.3 ports.

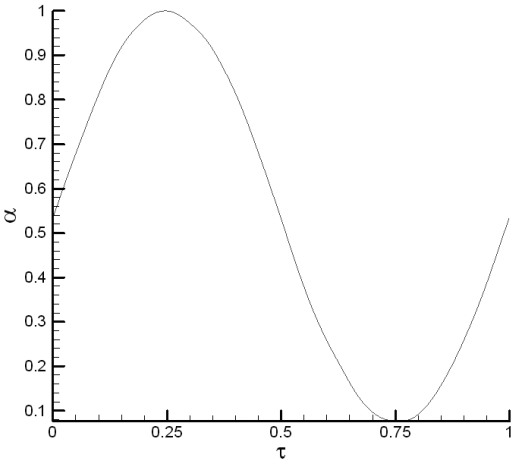

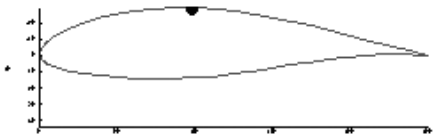

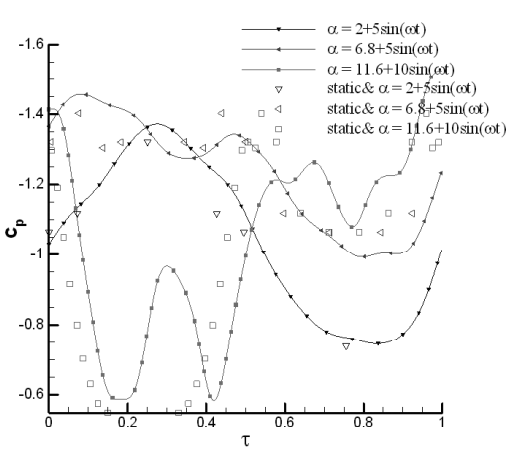

(a) variations of C_p vs τ

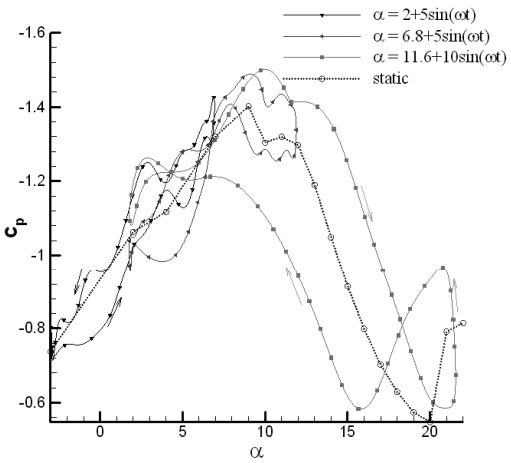

(b) variation of C_p vs α

i) upper

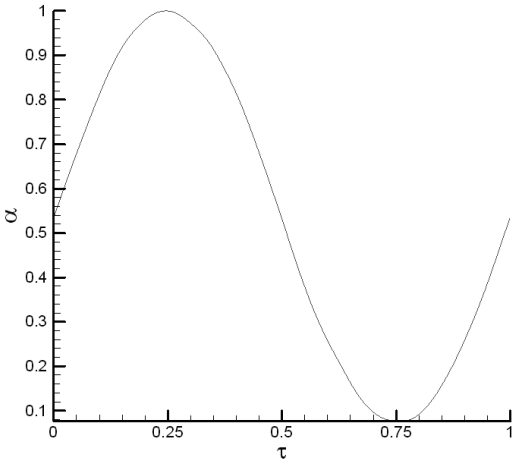

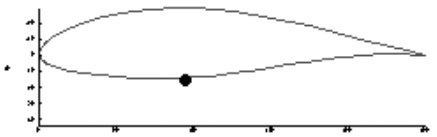

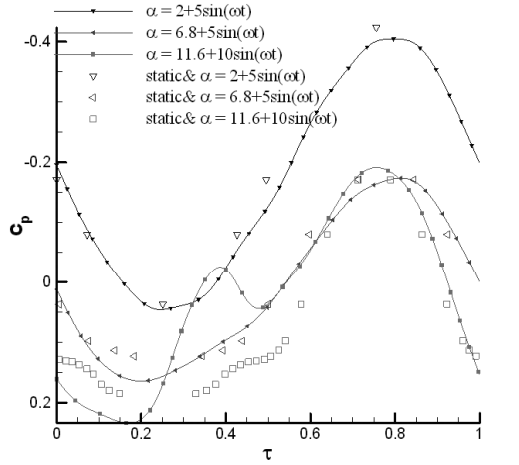

(c) variation of C_p vs τ

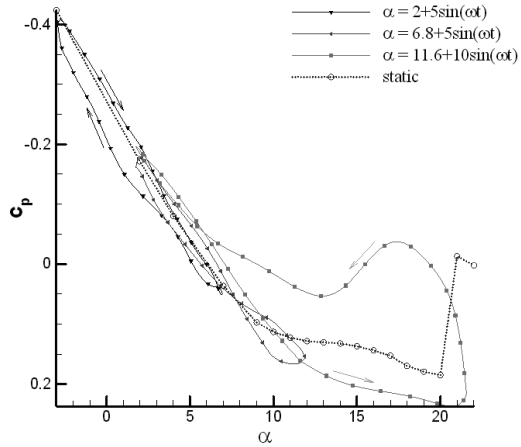

(d) variation of C_p vs α

ii) lower

Figure 8. Static and dynamic variations of pressure for the x/c=0.4 ports.

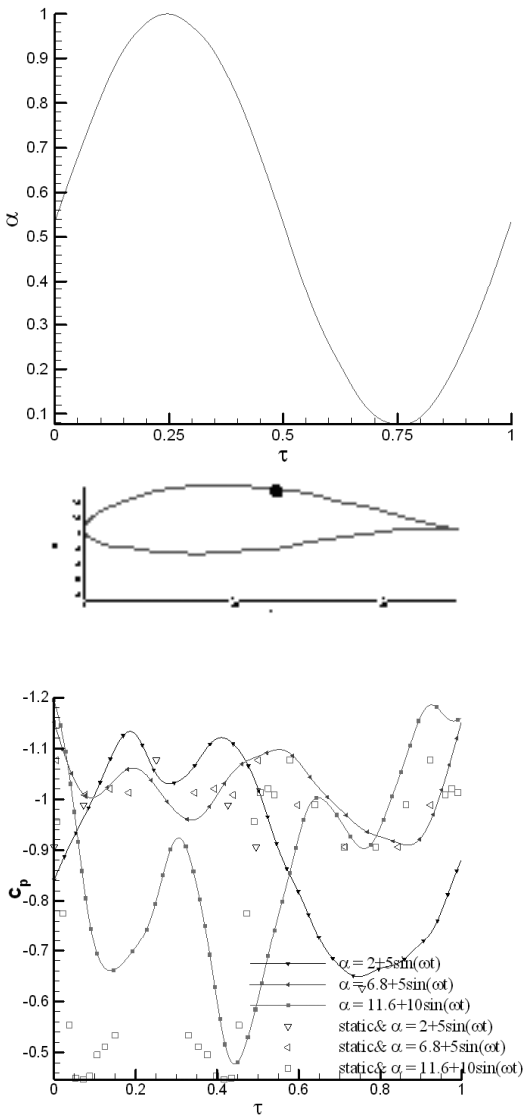

(a) variations of C_p vs τ

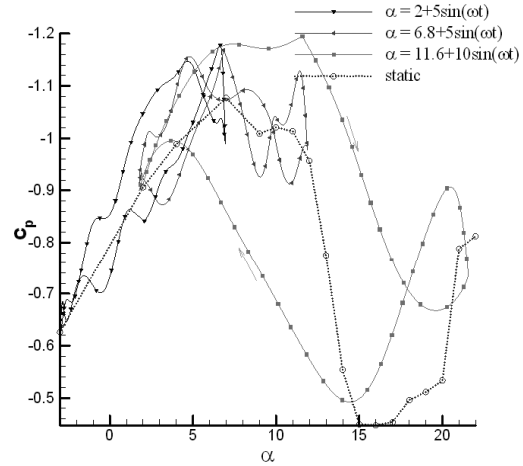

(b) variation of C_p vs α
i) upper

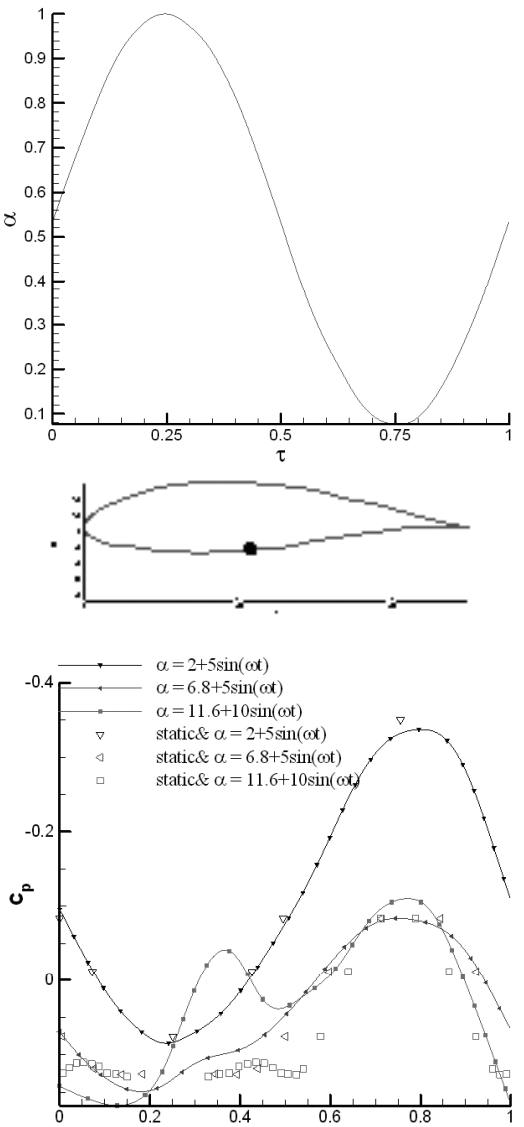

(c) variation of C_p vs τ

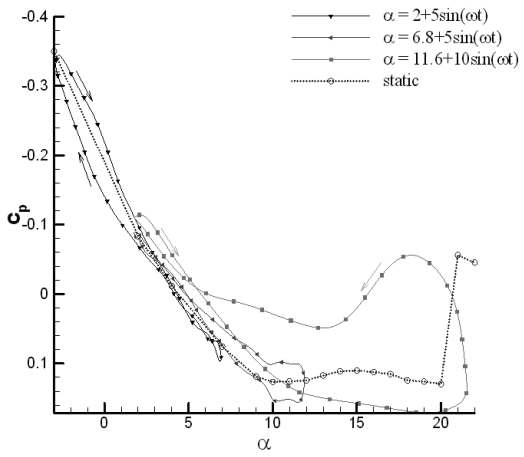

(d) variation of C_p vs α
ii) lower

Figure 9. Static and dynamic variations of pressure for the x/c=0.5 ports.

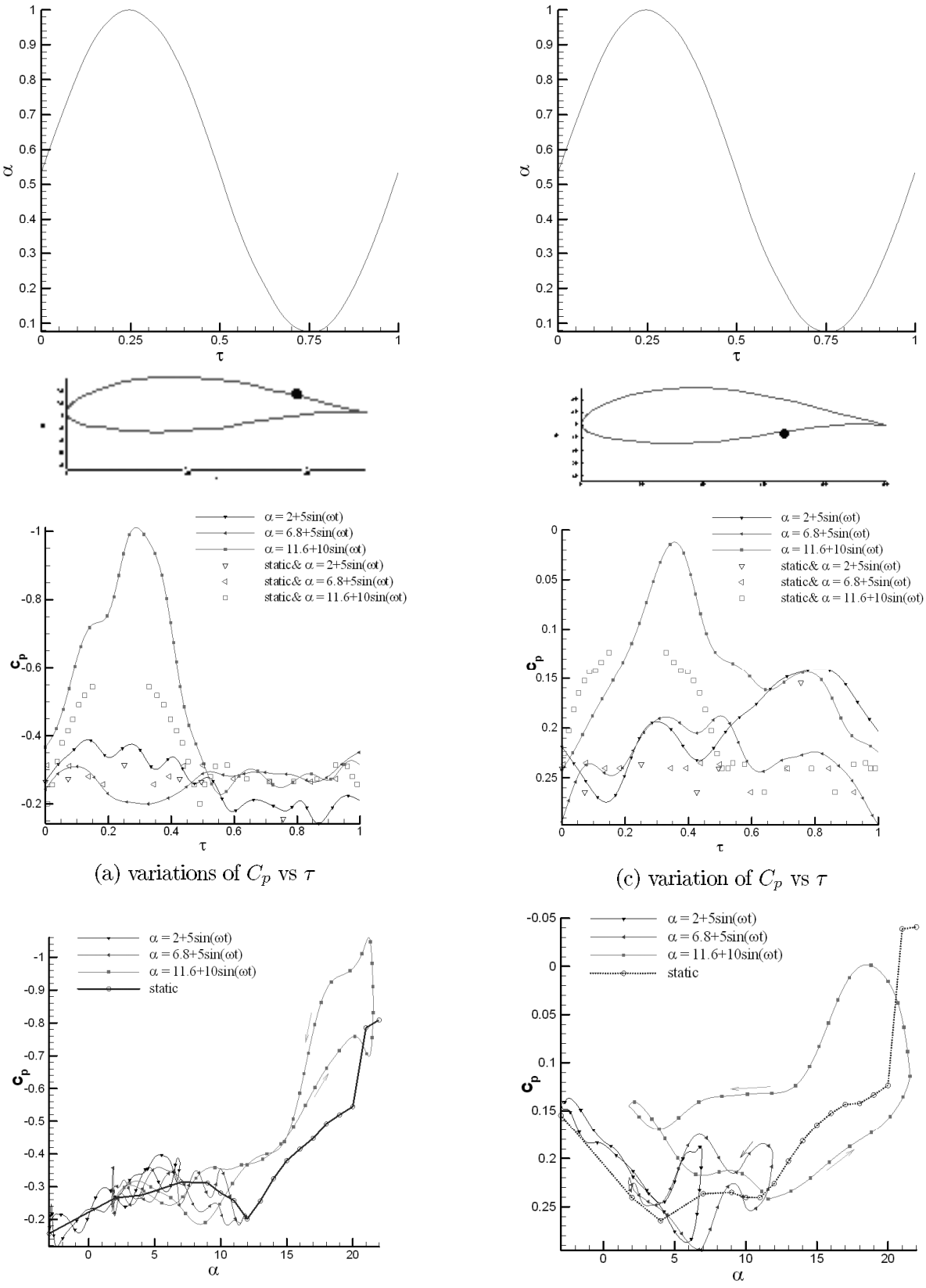

(a) variations of C_p vs τ

(c) variation of C_p vs τ

(b) variation of C_p vs α
i) upper

(d) variation of C_p vs α
ii) lower

Figure 10. Static and dynamic variations of pressure for the x/c=0.75 ports.

not the same. For the $\frac{x}{c} = 0.05$ port (Figure 5d), the cross over occurs at $\cong$ 14 degree while, for the $\frac{x}{c} = 0.15$ port, it happens at $\alpha = 11$ degree (Figure 6d). Figures 7 through 9 show similar variations as those of previous figures, but for pressure ports located at $\frac{x}{c} = 0.3$ to $\frac{x}{c} = 0.5$, for both upper and lower surfaces. Again static data show that $|C_{p_{\max}}|$ decreases as $\frac{x}{c}$ increases and the angle of attack where $|C_p|$ reaches its maximum value decreases too. Variations of the static pressure signature differ for each port as seen from these figures. It is seen that for the $\frac{x}{c} = 0.4$ port, $|C_p|$ decreases from $\alpha = 9$ to $\alpha = 20$ degrees (Figure 8b), beyond which it rises sharply, however, for the $\frac{x}{c} = 0.5$ port, the rise of $|C_p|$ occurs beyond $\alpha = 15$ but with a slower rate, (Figure 9b). Moreover, figure 9b shows that $|C_p|$ rises sharply when α is increased beyond 20 degrees similar to that of figure 8b.

Dynamic variations of C_p 's for all three ports and for the first two mean angles of attack $\alpha_{mean} = 2$ and 6.8 degrees are very irregular for the $\frac{x}{c} = 0.4$ and 0.5 ports (Figures 8b and 9b), while those of the $\frac{x}{c} = 0.3$ port (Figure 7b), are somehow similar to the corresponding cases shown in the previous figures. For the other two cases, $\frac{x}{c} = 0.4$ and 0.5, the dynamic values of C_p for the α_{mean} =2 and 6.8 degrees are within the ranges of the static values, but their variations during the upstroke and downstroke motions are not smooth (Figures 8b and 9b).

These three figures clearly show that as $\frac{x}{c}$ increases the absolute value of the pressure signatures for both static and dynamic motions for all ports as well as their behavior during increasing and decreasing angle of attack vary significantly.

For the highest α_{mean} case, the hysteresis loop does not form a figure eight shape as it did before. Rather, it crosses three points, forming three distinct loops (Figures 7b-9b). The width of these loops are different, with the middle loop having a wider width than the other two. Furthermore, the data show that as $\frac{x}{c}$ increases, the first hysteresis loop, low alpha case, begins to diminish until at $\frac{x}{c} = 0.5$, the loop for $\alpha_{mean} = 11.6$ degrees again forms a figure eight shape (Figure 9b). The trends of dynamic C_p variations for the corresponding lower surface pressure ports are shown in figures 7 through 9, ii. Even though $|C_{p_{\max}}|$ for all three cases have been reduced significantly in comparison to the previous figures, the shapes of the loops are still similar (Figures 7d-9d). However, for the highest α_{mean} cases the loops for all ports are wider and form figure eight shapes similar to those of the upper surface ports shown before. Similar cases are shown in figure 10 for the $\frac{x}{c} = 0.75$ ports, upper and lower surfaces. Static pressure data show that $|C_{p_{\max}}|$ is very small in comparison to the previous figures.

C_p reaches its maximum value at about $\alpha = 8$ degrees, beyond which its absolute value decreases (Figure 10b). However, $|C_p|$ starts to increases when $\alpha \geq 12$ degrees (Figure 10b). Variations of dynamic C_p 's for all cases are very irregular and cross each other at several angles of attack. It seems that most of the lift generated by this airfoil as it oscillates through various mean angles of attack and amplitudes, is due to the first 40 percent portion of the airfoil, $\frac{x}{c} \leq 0.4$. The flow over the rest of the model is either separated or does not produce a significant lift as seen by the pressure variations of each ports examined here. In figure 11 static and dynamic variations of C_p for the trailing-edge port for different cases mentioned before are shown. Static data show that C_p is positive, $C_p \cong 0.16$ and is almost constant from $\alpha = -3$ to 11 degrees (Figure 11b). By further increasing the angle of attack, C_p decreases nonlinearly up to the highest alpha tested in this study (Figure 11b). Variations of the dynamic C_p 's are different $\alpha = 11.6 + 105\sin(\omega t)$ as seen from figure 11b. It is seen by inspection that for the two lowest mean angles of attack, $\alpha_{mean} = 0.2$ and 6.8 degrees, C_p is almost constant, near zero, as the model oscillates through different angles of attack. For the highest mean angle of attack case, however, C_p variations form a figure eight hysteresis loop, but its value at various angles of attack is much different than the corresponding static values (Figure 11b).

Figure 12 shows pressure variations vs $\frac{x}{c}$ for the aforementioned α_{mean} 's and amplitudes and at four different angles of attack. The data for each case are for both upstroke and downstoke motions, but at the same angle of attack. For example, the oscillatory data shown in Figure 12a are for three different mean angles of attack and amplitudes, but all at the same case; i.e. $\alpha = 2°$ in the upstroke portion, Figure 12a,i, and $\alpha = 2°$ in the downstroke portion of the motion, Figure 12a, ii. Similar cases but for higher angles of attack, $\alpha = 4 - 11.6$ degree, are shown in Figure 12, b-d. Figure 12 a shows that for the 2 degrees angle of attack in both upstroke and downstroke motions flow remains attached for $\alpha_{mean} = 2$ and 6.8 degrees, but the flow is separated near the trailing-edge, $\frac{x}{c} > 0.75$ of the $\alpha_{mean} = 11.6$ degree case, Figure 12 a. Static data are higher, absolute value, in the upstroke motion for the low mean angle of attack ones, from $\frac{x}{c} = 0$ to $\frac{x}{c} = 0.5$ and vice-versa in the downstroke motion.

For the α=4 degree cases, Figure 12b shows a similar trend, but here the absolute value of the static pressure signature is higher in the upstroke motion for all mean angles of attack from $\frac{x}{c} = 0$ to $\frac{x}{c} = 0.3$. However, in the downstroke motions, the situation reverses. For the $\alpha = 11.6$ degrees case, Figure 12d shows that the static pressure signature is lower than the corresponding dynamic values for both mean angles of attack shown here. Moreover, this figure shows that in contrast to the previous figures, the flow over the model oscillating at $\alpha_{mean} = 11.6$ degree is not

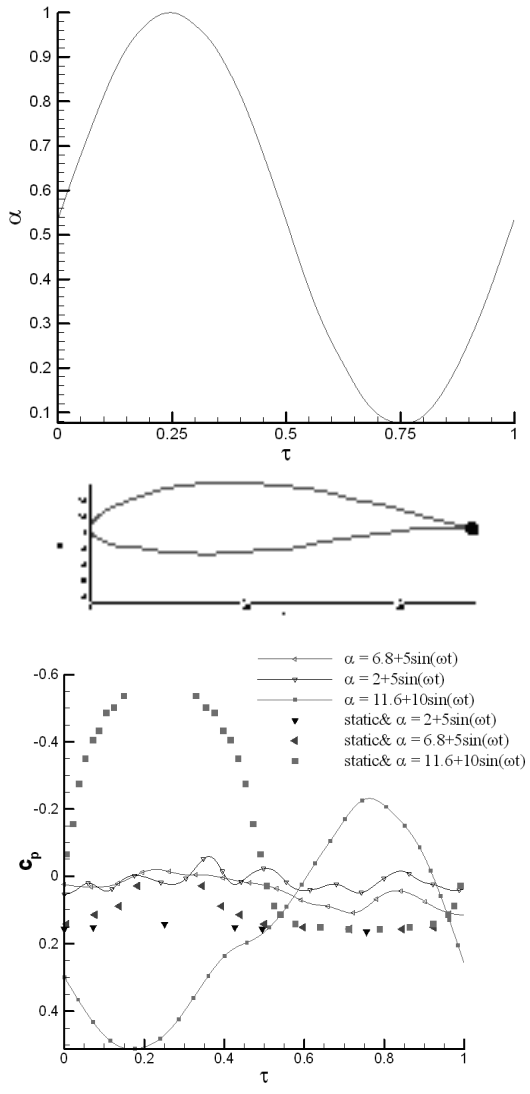

(a) variations of C_p vs τ

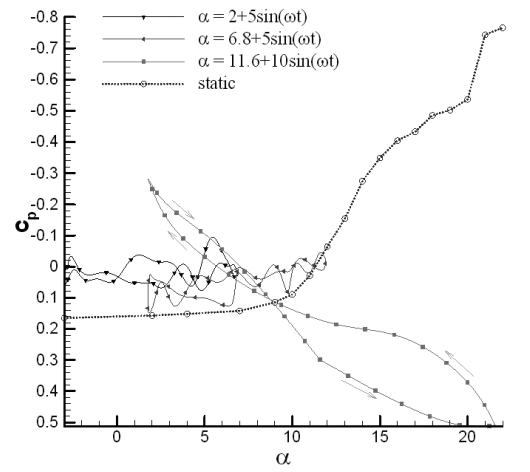

(b) variation of C_p vs α

Figure 11. Static and dynamic variations of pressure for the trailing-edge port.

separated in both upstroke and downstroke motions. However static $|C_p|$ is higher than the dynamic one, $\alpha_{mean} = 11.6$ degree, during the entire downstroke portion of the motion. Figure 13 shows the distribution of pressure over both upper and lower surfaces for three different cases examined here. For plotting clarity, the model pressures were unwrapped about the trailing-edge. The upper surface pressures are depicted on the right of the surface plot, while the lower surface valves are on the left. The trailing edge is then at the mid point of the x axis with the leading edge at each extreme. The non-dimensional time scale corresponds to angle of attack and its variation is shown on top of the figure too.

Figure 13a shows that $|C_{p_{\max}}|$ occurs at and near the leading edge portion of the model, however, the flow remains attached over the entire model throughout the motion, both upstroke and downstroke. Pressure variations for the upper surface are larger than the lower surface as seen from this figure. For the next case, $\alpha = 6.8+5\sin(\omega t)$, figure 13b shows that pressure peaks for the upper surface are much higher that those of figure 13a. However, dynamic pressure variations on the lower surface are small in comparison with those of Figure 13a. It seems that for this case slight flow separation exists near, and at the trailing edge of the model (Figure 13b). As seen from this figure, the differences in the pressure values for the upper and lower surfaces are large and most of the lift is generated by the first 35 percent of the model, $0 < \frac{x}{c} \leq 0.35$.

For the highest mean angle of attack and amplitude case tested here, dynamic C_p data show large suction peaks in the leading edge region as seen before (Figure 13c). From this figure it is clear that the flow behavior for these ranges of angles of attack is different than the corresponding cases shown in (Figure 13 a, b). The pressure over the entire lower surface seems to be almost constant with small variations with increasing or decreasing angles of attack, (Figure 13c). For the upper surface, however variations of C_p with angle of attack are significant and large peaks followed by deep valleys are seen. These differences create wide hysteresis loops seen previously. Finally figure 14 shows variations of the dynamic lift coefficient with an angle of attack for a reduced frequency of K= 0.04, Reynolds number of 0.4×10^6, and for the aforementioned mean angles of attack and amplitudes. Static data are also shown for comparison. The lift coefficient variations shown in this figure for both static and dynamic cases are obtained by integration of the static pressure distribution over the upper and lower surfaces of the model, 64 pressure ports, at various angles of attack. This figure shows that static c_l increases linearly from $\alpha = 2$ to $\alpha = 8$ degrees. Beyond $\alpha = 8$ degrees c_{l_α} decreases, which indicates that flow separation covers a portion of the model upper surface from the trilling

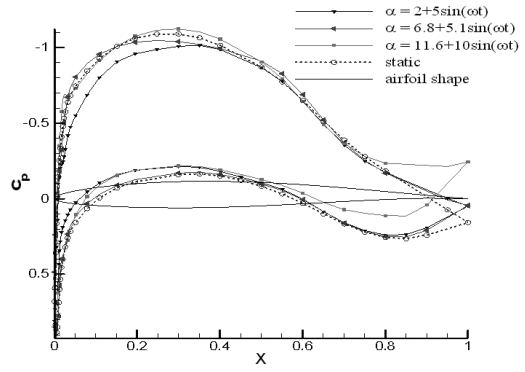

(i) upstroke

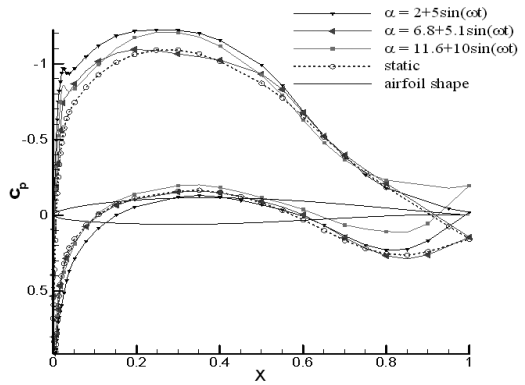

(ii) downstroke

(a) α=2°

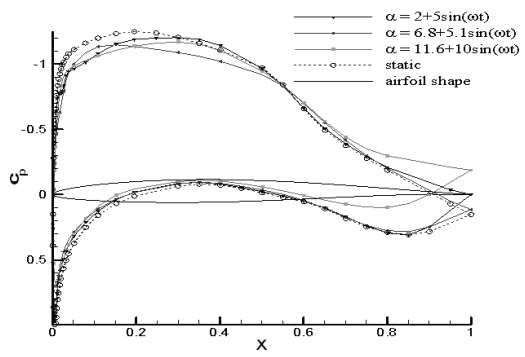

(i) upstroke

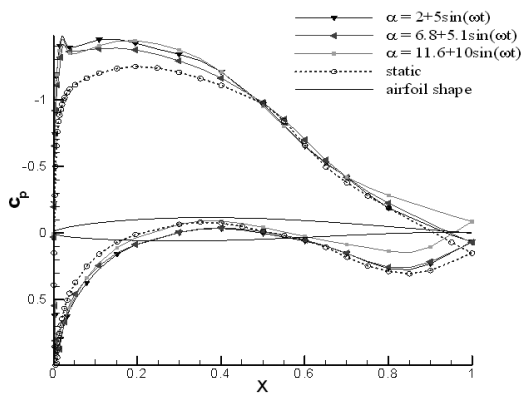

(ii) downstroke

(b) α=4°

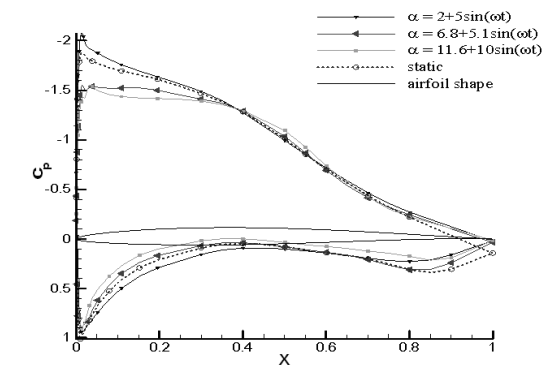

(i) upstroke

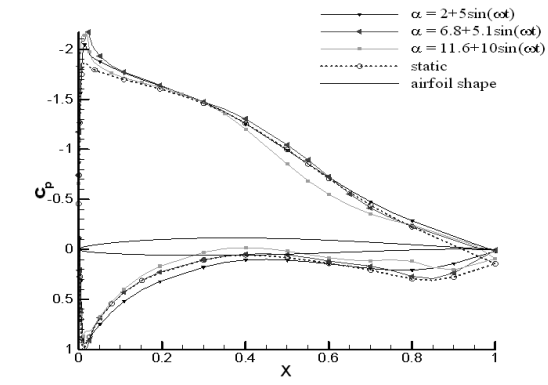

(ii) downstroke

(c) α=7°

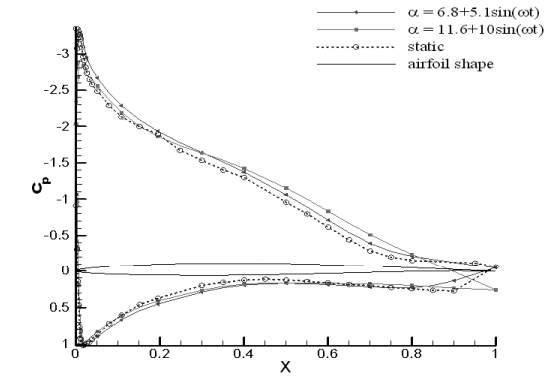

(i) upstroke

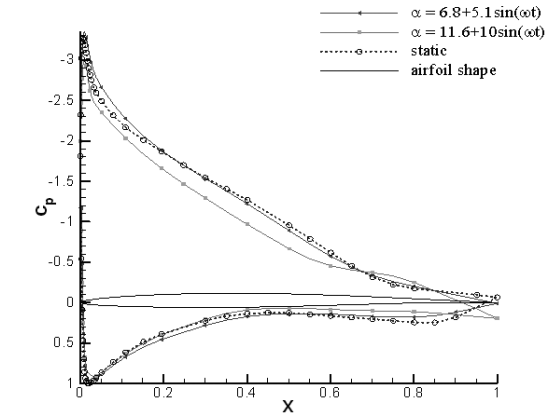

(ii) downstroke

(d) α=11.6°

Figure 12. Variations of static and dynamic pressure with x/c for different angles of attack.

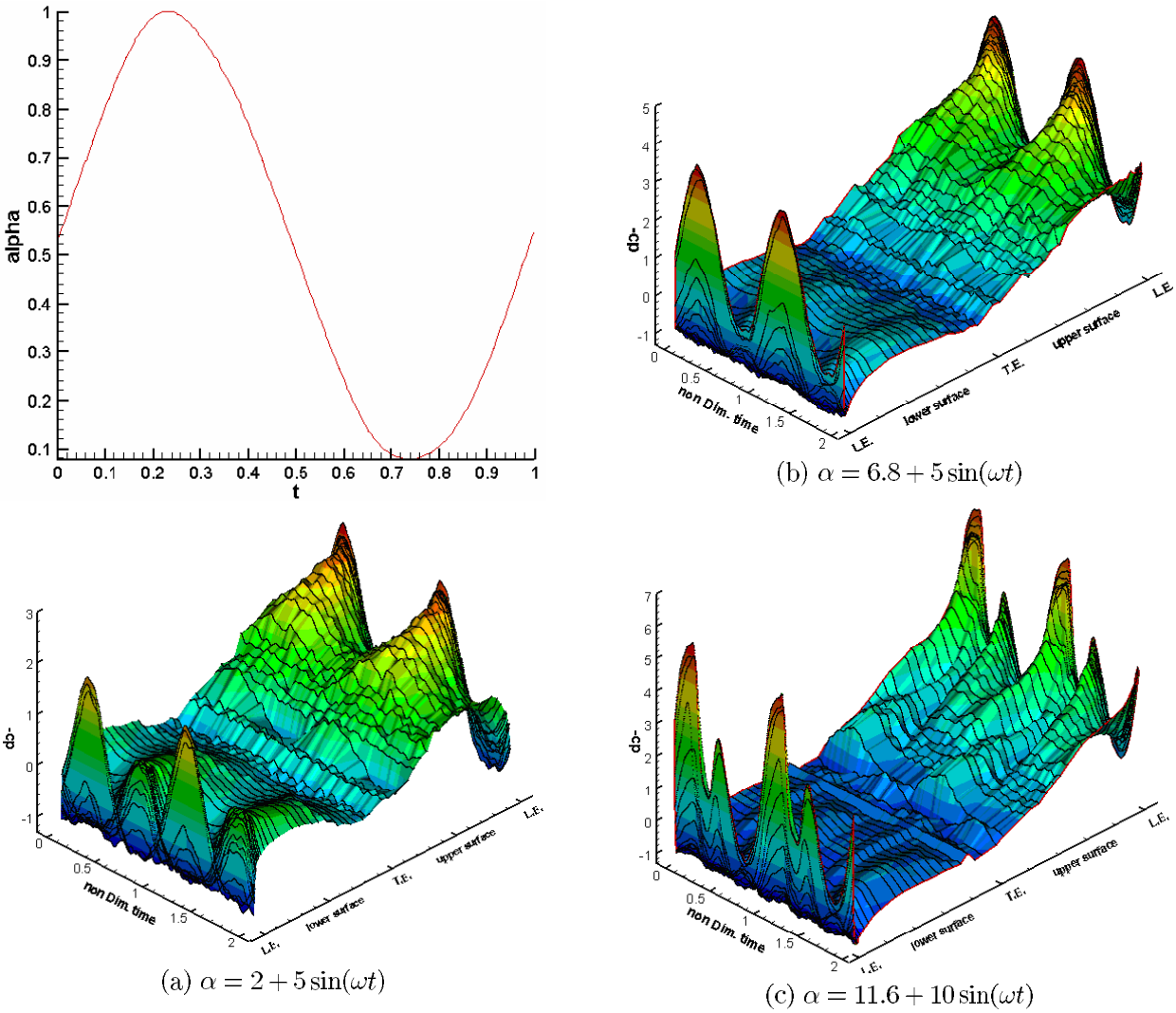

(a) $\alpha = 2 + 5\sin(\omega t)$ (b) $\alpha = 6.8 + 5\sin(\omega t)$

(c) $\alpha = 11.6 + 10\sin(\omega t)$

Figure 13. Unsteady pressure distributions, upper and lower surfaces, k=0.04.

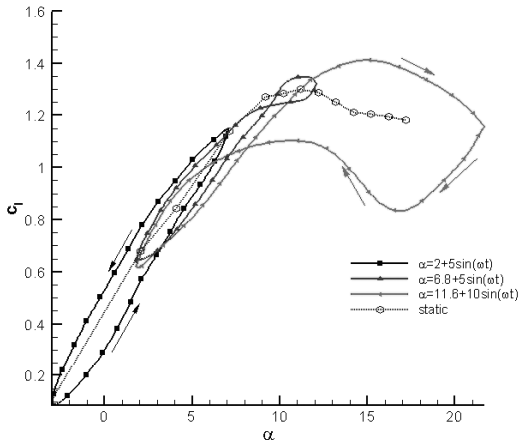

Figure 14. Static and dynamic variations of lift coefficient with angle of attack, k=0.04.

edge toward the leading edge. This phenomenon was seen in the pervious figures (Fig 12d), where the static c_p was constant from $\frac{x}{c} = 0.8$ to $\frac{x}{c} = 1$, at an angle of attack of 11.6 degrees. For this model and at this Reynolds number, $c_{l_{\max}}$ occurs at an angle of attack of about 11.5 ° and with further increase of α, c_l reduces, however the stall characteristic is very smooth (Fig. 14). For the dynamic oscillatory motions, variations of c_l with angle of attack are a strong function of α_{mean}, and amplitude as expected. For the lowest α_{mean} case, Figure 14 shows that during the entire upstroke motion, the dynamic c_l is lower than the corresponding static for all angles of attack, α = -3 to $\alpha = 7$ degrees i.e. dynamic c_l lags its corresponding static values. However, the situation reverses in the downstroke portion of the motion, where the dynamic c_l leads its corresponding static values for α = 7 to α = -3 degrees hence forming a hysteresis loop in the data. The shape of the hysteresis loop for this motion is of ellipsoidal shape, very close to those of pressure ports located at $\frac{x}{c} < .4$ mentioned before. Variations

of c_l with alpha for most of the upstroke portion of the motion are almost linear while during the downstroke motion c_l varies non-linearly (figure 14). As the mean angle of attack increases, $\alpha = 6.8 + 5\sin(\omega t)$, dynamic variation of c_l with angle of attack differs from that of the previous case, $\alpha = 2 + 5\sin(\omega t)$. It is seen by inspection that the hysteresis loop for this motion forms a figure eight shape where in the upstroke part of the motion dynamic c_l lags its corresponding static value, from $\alpha = 1.8$ to $\alpha = 9$ degrees, and for the rest of the motion $\alpha \cong 9$ to $\alpha \cong 11.8$ degrees, dynamic c_l leads its corresponding static values (Figure 14). In the downstroke motion, however, dynamic c_l lags static ones from $\alpha = 11.8$ to $\alpha = 7$ degrees and leads for the rest of the motion. The maximum dynamic c_l for this motion is slightly higher than the $c_{l_{\max}}$ for the steady state case and it seems that the differences would have been higher if the amplitude had been larger. Variations of the dynamic c_l with the angle of attack for the $\alpha = 11.6 + 10\sin(\omega t)$ case also form a figure eight shape and the cross-over point occurs at $\alpha = 8$ degrees (Figure 14). Again dynamic c_l in the upstroke motion lags its corresponding static value from α =1.6 to $\alpha = 11.5$ degrees and leads for the rest of the motion, $\alpha = 11.5$ to $\alpha = 21.6$ degrees.

Dynamic stall angle of attack for the present case occurs at α =15 degrees with $c_{l_{\max}}$ reaching a value of about 1.42 while for the static case this happens at α =11.5 degree and $c_{l_{\max}}$ =1.3. Therefore, it is seen that even for this low oscillation frequency, note that for this k, most authors indicate that the flow is in the quasi steady case and not fully dynamic ones, and that an overshoot of about 9 percent in the lift and 30 percent in the corresponding angle of attack is obtained. In the downstroke portion of the motion, flow remains separated over the airfoil until an angle of attack of about 17 degrees, where the flow starts to reattach from the leading-edge toward the trailing-edge of the model. Dynamic c_l in the decreasing angle of attack portion of the motion lags its corresponding static values for all angles of attack down to $\alpha \cong 5$ degrees where flow reattaches over almost entire upper surface of the model. For $\alpha < 5$ degrees, dynamic c_l leads its corresponding static ones slightly (Figure 14). The shape of the hysteresis loops for this amplitude, $\alpha = 11.6 + 10\sin(\omega t)$, for the low alpha case is again similar to an ellipse, but that of the high alpha one, $8 \leq \alpha \leq 22$, is wide and does not resemble any known geometrical shape.

CONCLUSION

An extensive experimental study was conducted to investigate the flow phenomena over a section of a 660 kW wind turbine blade, undergoing static and dynamic oscillatory motions. Surface pressure distributions at 64 points over and below the model were measured. Our study included the effects of Reynolds numbers, reduced frequency, mean angles of attack and amplitudes on the pressure distribution over the model. In this paper only effects of mean angles of attack and amplitude on the dynamic pressure distribution at a constant reduced frequency and Reynolds number were presented. Static data are also shown for comparison. Highlights of the experimental findings include:

- Mean angle of attack and amplitude had considerable effects on the dynamic pressure. For the low α_{mean} cases, dynamic C_p 's in the upstroke motion were less than their analogous static values. Moreover, their values in the downstroke motion were larger than their corresponding static values.
- At higher mean angles of attack and amplitudes, large overshoot in the dynamic C_p 's were observed and the dynamic stall angle of attack increased considerably.
- By examining the character of the flow at each pressure port, it was seen that the pressure ports located at $\frac{x}{c} < 0.4$ had significant effects on the aerodynamic loads while the effects of those located at $\frac{x}{c} > 0.4$ and beyond were less important.
- Variations of the dynamic C_p 's for pressure ports located at $0 \leq \frac{x}{c} \leq 0.4$ are similar to those of the c_l vs. α plot. However, for ports located at $\frac{x}{c} \geq 0.4$, dynamic variations of C_p were very irregular.
- Static variations of c_l with angle of attack were linear for the low angles of attack and became non linear at moderate alphas.
- The hysteresis loop for the moderate to high alpha case formed a figure eight shape and the cross over point varied with the mean angle of attack and amplitude.
- Dynamic stall angle of attack even for this low reduced frequency motion occurred at a higher angle of attack than that of the static case with higher dynamic $c_{l_{\max}}$.
- In the downstroke motion, however, flow remained separated over the model until an angle of attack much lower than the static α max.

Further study regarding the effects of Reynolds number, trip strip, and reduced frequency are undergoing and will be presented later on.

REFERENCES

1. Maresca, C., Favier, D., and Rebont, J., "Experiments on an Airfoil at High Angle of Incidence in Longitudinal Oscillations", *Journal of Fluid mechanics*, **92**, PP 671-690(1979).

2. Broeren, A. P., and Bragg, M. B., "Spanwise Variation in the Unsteady Stalling Flowfields of Two-Dimensional Airfoil Models", *AIAA Journal*, **39(9)**, PP 1641-1651(2001).
3. Walker, J. M., Helin, H. E. and Chow, D. C., "Unsteady Surfaces Pressure Measurement on a Pitching Airfoil", *AIAA-85-0532*, AIAA Shear Flow Control Conference, (1985).
4. Leishman , J. G., "Challenges in Modeling the Unsteady Aerodynamics of Wind Turbines", *AIAA 2002-0037*, 21th ASME Wind Energy Symposium and the 40th AIAA Aerospace Sciences Meeting, (2002).
5. Wallace, C. P., "Is It a Breeze? ", *Time Magazine*, PP 36-37(2002).
6. Younsi, R., El-Batanong, I. Tritsch, J., Naji, H., and Landjerit, B., "Dynamic Study of a Wind Turbine Blade with Horizontal Axis", *J. Mech. A/Solids 20*, PP 241-252(2001).
7. Huyer, S. A., Simms, D. A., and Robinson, M. C., "Unsteady Aerodynamics Associated with a Horizontal-Axis Wind Turbine", *AIAA Journal*, **34(7)**, PP 1410-1419(1996).
8. Modi, V. J, and Fernando, M. U. K., "On the Performance of the Savonius Wind Turbine", *Journal of Solar Energy Engineering* , **111**, PP 71-81(1989).
9. Vries, O. D., "On the Theory of the Horizontal-Axis Wind Turbine", *Annual Review of Fluid Mechanics*, **15**, PP 77-96(1983).
10. Johansen, J., "Prediction of Laminar / Turbulent Transition in Airfoil Flows", *Riso-R-987 (EN)*, Riso National Laboratory , (1977).
11. Soltani, M. R., Dehghan-Manshadi, M. ,and Mirabdollahi, M., "Turbulent Reduction in Wind Tunnel Using a Trip Strip", *HT-FED 2004-56876*, ASME Heat Transfer/Fluid Engineering, U.S.A , (2004).
12. Soltani, M. R., Askari, F., and Bakhshalipour, A., "Roughness and Turbulence Effects on the Aerodynamic Efficiency of a Wind Turbine Blade Section", *AIAC-2005-057*, 2th Ankara International Aerospace Conference , (2005).
13. Soltani, M. R., Rasi, F., Seddighi, M., and Bakhshalipour, A., "An Experimental Investigation of Time Lag in Pressure Measuring System", *AIAC-2005-028*, 2th Ankara International Aerospace Conference, (2005).
14. Rae, W. H., and Pope, A., *Low Speed Wind Tunnel Testing*, secondEd., John Wiley and Sons, (2000).